Dressed topological edge states in HgTe-based 2D topological insulators

Matthieu C. Dartiailh,[1] Simon Hartinger,[2] Alexandre Gourmelon,[1] Kalle Bendias,[2] Hugo
Bartolomei,[1] Jean-Marc Berroir,[1] Gwendal Fève,[1] Bernard Plaçais,[1] Lukas Lunczer,[2]
Raimund Schlereth,[2] Hartmut Buhmann,[2] Laurens W. Molenkamp,[2] and Erwann Bocquillon[1]

[1]*Laboratoire de Physique de l'École Normale Supérieure, ENS,*
PSL Research University, CNRS, Sorbonne Université, Université Paris Diderot,
Sorbonne Paris Cité, 24 rue Lhomond, 75231 Paris Cedex 05, France
[2]*Physikalisches Institut (EP3), Am Hubland, Universität Würzburg, D-97074 Würzburg, Germany*
(Dated: April 1, 2019)

Enormous efforts are focused on the edge states of two-dimensional topological insulators currently, motivated by exotic fundamental physics, robust topological quantum computation and novel spinorbitronics. Progress is however largely impeded by the fragility of the edge states visible only on short lengths. In this context, microwave transport allows us to capacitively probe the density of states of HgTe topological insulators while measuring simultaneously the device resistance. Besides bulk states, the dynamical transport highlights the responses of the edges, which host very mobile carriers, but are also much denser than theoretically expected. We propose a scenario of 'dressed' topological edge states, with topological edge carriers coupled to neighboring confined bulk states. These additional states thus contribute to the large density of states at the edges and may participate to the fragility of topological edge states by causing additional scattering.

INTRODUCTION

Promising platforms have emerged to investigate the physics of two-dimensional topological insulators, which exhibit the quantum spin Hall (QSH) effect. The most prominent examples are HgTe quantum wells, in which many transport signatures of the QSH effect have been observed[1–5] as well as a fractional Josephson effect, a signature of topological superconductivity[6,7], in HgTe-based Josephson junctions. Another promising material system, InAs/GaSb double quantum well, also shows the quantized conductance that accompanies topological edge state transport[8,9]. Several other layered materials are also currently under development, such as bismuthene[10] or WTe$_2$[11].

However, the progress in the study of the QSH effect has been severely hampered by the relative fragility of the edge states, which are only visible on lengths of a few microns despite the expected topological protection[1,9,12]. A large number of scenarios have been constructed to explain this behaviour[13–17], which for example rely on two-particle scattering or disorder. It is consequently of utmost priority to experimentally investigate the physics of topological quantum wells and identify the main sources of scattering. In this context, dc transport has, to date, offered limited insights. Microwave ac signals enable simultaneous measurements of the capacitive response, sensitive to the density of electronic states, as well as the resistive response, probing their ability to conduct, as exemplified recently in three-dimensional topological insulators[18–21]. The microwave response thus naturally evidences the resulting RC charge relaxation times of each transport channel, allowing to isolate them.

Here, we report on the microwave capacitance spectroscopy, in the frequency range 10 kHz–10 GHz, to investigate narrow HgTe quantum wells (QW). The conduction and valence bands of the QW are ruled by a single-mode bulk response, which is accurately described by **k.p** band structure predictions. In contrast the microwave spectrums exhibit striking two-mode dynamics when the Fermi level approaches the gap. Combining these observations with geometrical scalings, we identify these two modes as bulk and edge carriers, and characterize their respective dynamical transport properties. Near the gap, a major part of the high observed DOS signals charge puddles in the bulk, which have a low conductance and slow dynamics. Besides, a one-dimensional contribution is clearly visible and attributed to the edges of the sample. The edges host very mobile carriers but are also much denser than theoretically expected for pure helical edge states. The microwave dynamical transport thus strongly suggests the presence of "dressed" topological edge states. Most likely, the dressed topological edge states originate from bare helical edge states, dressed with other bulk states that are confined near the edge by electrostatics and/or disorder. The latter do not participate efficiently to transport but rather introduce additional scattering. The scenario is intrinsically related to the presence of helical edge states, and provides a potential original explanation for the observe fragility of topological edge states.

RESULTS

Sample geometry and experimental techniques

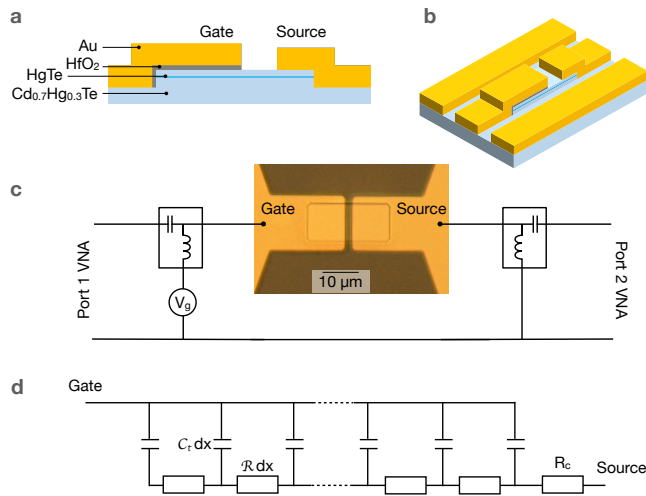In this first section, we describe the samples and the admittance measurement setup. The samples are based

FIG. 1. **Experimental techniques:** a) Schematic side view of the device, showing the different layers of the Cd-HgTe/HgTe heterostructure, as well as the gate and contact. b) Artist view of the capacitor device, embedded in a coplanar waveguide c) High-frequency measurement setup, based on a vector network analyzer (VNA), the ports of which are connected to both source and gate. Two bias-tees are used to apply the dc gate voltage V_g that controls the electron density. For low frequency measurements, a lock-in replaces the VNA. d) Model of the capacitor as a distributed RC line, with a contact resistance R_c, and a linear resistance $\mathcal{R}$ and linear capacitance $\mathcal{C}_t$.

on HgTe/HgCdTe quantum wells grown by molecular beam epitaxy on CdTe substrates. The thickness t of the quantum wells varies between 5 and 11 nm, while the protective HgCdTe capping layers has a typical thickness of 15 nm. In these quantum wells, the band structure consists of light electrons in the conduction band, and heavier holes in the valence band. A topological phase transition occurs for the critical thickness $t_c \simeq 6.3$ nm. For $t > t_c$ an inverted band ordering is responsible for the appearance of topologically protected quantum spin Hall edge states in the gap of the quantum well[22]. For $t < t_c$, the band ordering is normal and no edge states occurs, the sample is topologically trivial. The quantum wells are first characterized using standard Hall-bar measurements, which yield mobilities around $2 \times 10^5 \,\mathrm{cm^2\,V^{-1}\,s^{-1}}$ and densities of $3 \times 10^{11} \,\mathrm{cm^{-2}}$ in the conduction band. Though more layers have been investigated and have given similar results, we focus in this article on two topological samples (Topological A and B). Topological A (resp. B) has a thickness of 10.6 nm (resp. 8 nm) and a predicted gap $\lesssim 2$ meV (resp. 8 meV) as shown in Fig.2. A reference non-inverted sample is provided by a 5.8 nm-thick QW (predicted gap 20 meV) denoted Trivial. On each layer, we investigated devices made of square capacitors of side $L = 3, 5, 10, 20\,\mu\mathrm{m}$, embedded in a gold coplanar waveguide (see Fig.1a and 1b). For these devices, the capacitor mesa is defined via a wet etching technique[12] that preserves the high crystalline

quality and the high mobility of the epilayer. The contacts and gate are patterned via optical lithography. The gold gate electrode is evaporated on top of a 7 nm-thick HfO_2 insulating layer, grown by low-temperature atomic layer deposition (ALD)[12]. An ohmic contact is deposited by Au evaporation.

The capacitors are measured in a cryogenic RF probe station at a temperature $T = 10$ K, over a wide range of frequency f, using both a lock-in detector ($f < 1$ MHz) and vector network analyzer (VNA) in a range 10 MHz $< f < 20$ GHz. Earlier works[20,21,23] have demonstrated that the capacitors can be (assuming translation invariance along the transverse direction) described by a distributed RC line of length L, with line capacitance $\mathcal{C}_t$ and resistance $\mathcal{R}$, such as the one depicted in Fig.1d.

In the low-frequency range, measured either with the lock-in amplifier or the VNA (see Methods), the device is equivalent to a capacitor $C_t = \mathcal{C}_t L$. C_t is the series addition of the geometric capacitance C_g and the quantum capacitance C_q: $C_t^{-1} = C_g^{-1} + C_q^{-1}$. The former accounts for the energy cost required to induce a charge across the dielectric barrier, and depends on the electrostatic coupling between the gate electrode and the QW plane. The latter is accounts for the increase of the Fermi energy, which is sizable in low density electron systems It is simply given by $C_q = e^2\rho$, where ρ is the density of states (DOS), for weakly interacting systems in the limit of zero temperature. One then directly accesses C_t when measuring the out-of-phase response of the device, with the admittance given by $Y(\omega) = i\omega C_t$ to the lowest order in $\omega = 2\pi f$. One can readily obtain the geometric capacitance C_g by measuring C_t at high electron densities (optimally deep in the valence band), with a precision of typically 2%. Indeed, for high electron densities, C_t saturates $C_t \simeq C_g$ as $C_q \to \infty$ (see[20,23] and SI). Assuming C_g is constant, one can then obtain C_q which is the main quantity of interest in this work. Importantly, one can also compute the chemical potential[24] $\mu = \int^{V_g} \left(1 - \frac{C_t(V)}{C_g}\right) dV$ (we fix the origin $\mu = 0$ in the gap, identified as the peak of resistance, see below). As a consequence, it is possible to compare the DOS $\rho(\mu)$, or more conveniently the areal quantum capacitance $c_q(\mu) = \frac{C_q(\mu)}{L^2}$, with predictions obtained from $\mathbf{k} \cdot \mathbf{p}$ calculations of the band structure of the QW, that we have performed following Ref. 25.

The next term in the low-frequency expansion of Y is given by the total resistance R_t resulting from the access resistance R_c and the finite sheet resistance of the HgTe film $R = \mathcal{R}L$ (see SI): $R_t = R_c + \frac{R}{3}$ such that the low frequency admittance is then given by $Y(\omega) = i\omega C_t + \omega^2 R_t C_t^2$. The measurement of R_t requires a proper phase reference, which can be obtained using a VNA. Standard in-situ calibration techniques enable to de-embed the response of the circuitry and stray capacitances from the admittance $Y(\omega)$ of interest. Beyond this low-frequency response described by the lumped $R_t C_t$ circuit, VNA measurements up to 20 GHz allow for a

complete characterization of the frequency response in regimes where the distributed nature of the HgTe film can be probed.
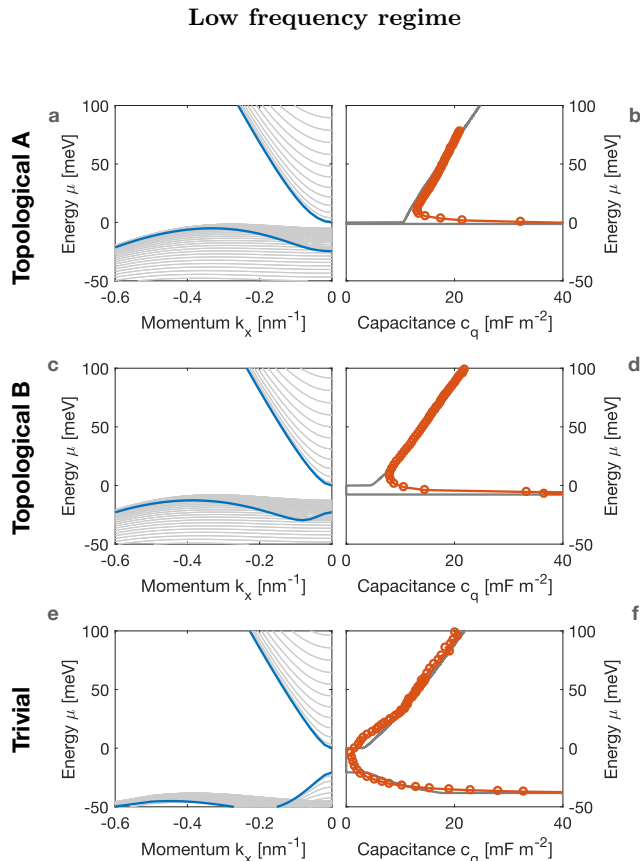
Low frequency regime

FIG. 2. **Quantum capacitance of HgTe quantum wells:** a, c, e) Energy spectrum as function of momentum k_x, as calculated from a $\mathbf{k} \cdot \mathbf{p}$ model of the three studied samples (Topological A, Topological B and Trivial). The blue lines correspond to the transverse momentum $k_y = 0$, the light grey lines to the subbands $k_y \neq 0$. b, d, f) Quantum capacitance c_q (per unit area) as function of energy μ for the same three samples (for a size of $L = 10 \,\mu\mathrm{m}$). The grey line corresponds to the computed value of c_q given the $\mathbf{k} \cdot \mathbf{p}$ band structure, the red lines correspond to experimental data.

This paragraph focuses on the low-frequency quantities R_t and C_t, and in particular establishes the existence of a 1D density of states in topological samples, as expected due to the presence of topological edge states. Following the above techniques, we compare experimental measurements of the quantum capacitance c_q as function of energy μ with $\mathbf{k} \cdot \mathbf{p}$ predictions for each type of sample, as presented in Fig.2. For all three samples, the capacitance is low (between 10 and $20 \,\mathrm{mF\,m^{-2}}$) in the conduction band ($\mu > 0$), and increases quasi-linearly with μ, as expected for two-dimensional bands with quasi-linear band dispersion. The agreement with $\mathbf{k} \cdot \mathbf{p}$ calculations is excellent in this regime, provided the value of C_g is fine tuned (see SI). In this regime, the quantum capacitance is

given by[20] $c_q = \frac{e^2}{\pi(\hbar v_F)^2}\mu$ which yields the Fermi velocity $v_F \simeq 0.8 - 1 \times 10^6 \,\mathrm{m\,s^{-1}}$. In the valence band ($\mu \ll 0$), we observe that c_q is very high ($c_q > 40 \,\mathrm{mF\,m^{-2}}$) as the valence band has a high mass. c_q is however difficult to extract with high precision in this range, due to the finite value of the geometric capacitance $c_g \simeq 3.9 \,\mathrm{mF\,m^{-2}}$. In between these two regimes, a minimum is observed in the data. It indicates the gap of the QW, clearly visible in the $\mathbf{k} \cdot \mathbf{p}$ calculations. For Trivial, the capacitance reaches a very low value, $c_q < 1 \,\mathrm{mF\,m^{-2}}$ and the QW is strongly depleted, as expected. In Topological A and B, $c_q \simeq 10 \,\mathrm{mF\,m^{-2}}$ in the gap, where QSH edge states should be observed. A modeling as merely one-dimensional edge states yields a quantum capacitance[26] of $\frac{4e^2}{hv_F} \simeq 0.2 \,\mathrm{nF\,m^{-1}}$ for the topological edge states. On a $L = 10 \,\mu\mathrm{m}$ device, it corresponds to a very low areal contribution $c_q < 0.1 \,\mathrm{mF\,m^{-2}}$, much smaller than the observed minimum. This residual contribution in the gap is thus unlikely to originate solely from the edge states, but more likely from disorder in the bulk bands. A rough modeling with a gaussian smearing of c_q gives a typical standard deviation of $20 \,\mathrm{meV}$ comparable to the gap scale, but much larger than the temperature ($kT \lesssim 1 \,\mathrm{meV}$) and any broadening induced by the probe signal. We thus attribute this smearing mechanism to inhomogeneous bulk bands, forming charge puddles due to disorder, thickness fluctuations[27] or inhomogeneous electrostatics. As a consequence of the extremely large DOS of the valence band, the minimum of c_q is surprisingly upshifted in energy with respect to the theoretically predicted gap (here typically around $\mu = 10 \,\mathrm{meV}$, with a reference $\mu = 0$ taken at the bottom of the conduction band).

In Fig.3, the total resistance R_t of Topological A is presented together with the quantum capacitance c_q. In the valence and conduction band, R_t is very low as the QW is very conductive, and saturates close to the value of the contact resistance, $R_t \simeq R_c$ (the latter being extracted from the high-frequency analysis, and depicted as the dashed line). The gap is clearly indicated by a sharp peak in R_t. For trivial samples (not shown), the gap is quite insulating and $R_t > 400 \,\mathrm{k\Omega}$. For topological samples in an ideal QSH regime, the geometry resembles that of a mesoscopic capacitor[28–30], and a charge relaxation resistance between $\frac{R_K}{4}$ (coherent regime) and $\frac{R_K}{2}$ (incoherent regime) is expected[31,32], where $R_K = \frac{h}{e^2}$ is the resistance quantum. Though many measured peak resistances lie in this range (see Fig.3), none of the samples however exhibit a clear quantized resistance plateau, and higher values ($\sim R_K$) are sometimes reached, probably due to the presence of scattering as the perimeters of the sample are large ($30 \,\mu\mathrm{m}$ here). Importantly, we found that in all samples the minimum of c_q and the maximum of R_t are not aligned. This indicates that the gap hosts a large amount of bulk states that do not participate very efficiently to transport, and that the Fermi energy is mostly pinned to the valence band. In contrast, the minimum of c_q (here around $\mu \simeq 10 \,\mathrm{meV}$) corresponds
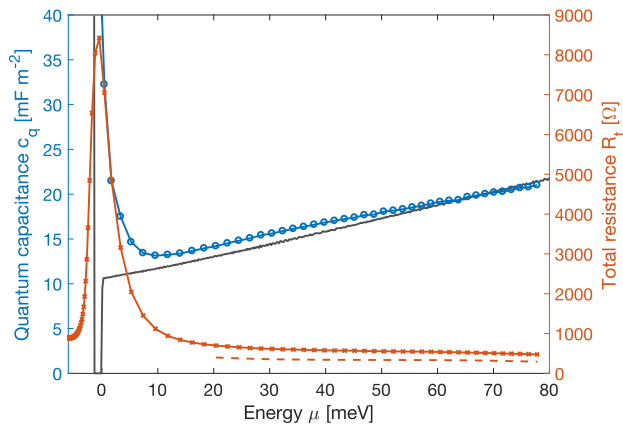
FIG. 3. **Quantum capacitance and resistance of a topological HgTe quantum well:** The quantum capacitance per unit area c_q (blue line, left axis) and the total resistance R_t (red line, right axis) are plotted as a function of energy μ. As a grey line, the computed value of c_q given the $\mathbf{k} \cdot \mathbf{p}$ band structure is also reproduced. As a dashed red line, the contact resistance R_c is plotted in the energy range in which it can meaningfully be extracted from the high-frequency analysis. This dataset has been measured on Topological A for $L = 10\,\mu\text{m}$.

to a smaller DOS, but a higher conductance.

So far, neither the quantum capacitance c_q nor the resistance R_t enable to directly identify the topological edge states. In the low-frequency regime, an additional parameter such as the dependence on length L is necessary. As a matter of fact, the contributions to the quantum capacitance should scale as $\propto L$ for one-dimensional edge states while two-dimensional bulk bands scale as $\propto L^2$, so that the areal quantum capacitance can be written as (see Methods):

$$c_q = c_q^{2D} + \frac{3c_q^{1D}}{L} \qquad (1)$$

with c_q^{1D} and c_q^{2D} the line and surface quantum capacitance. Varying L, we now investigate these scaling laws in Fig.4a, 4b, 4c. For Topological A and B all curves are superimposed for $\mu > 60\,\text{meV}$ signaling that c_q does not depend on L, and the system is thus two-dimensional. However, a clear length dependence appears for lower energies (Fig.4b and 4c). We observe that the quantum capacitance c_q can be written as the sum of a one-dimensional and a two-dimensional contribution. Fits of the data (see SI) for each μ finally yields c_q^{1D} and c_q^{2D}, plotted in Fig.4e and 4f. The two-dimensional part c_q^{2D} follows the $\mathbf{k} \cdot \mathbf{p}$ calculations, confirming the validity of the modeling. In contrast, the one-dimensional contribution c_q^{1D} appears at energies $\mu < 40\,\text{meV}$ and is at its largest near the gap. The order of magnitude $c_q^{1D} \simeq 5 - 10\,\text{nF m}^{-1}$ is however 25 to 50 times larger than that expected for a merely one-dimensional edge (typ. $0.2\,\text{nF m}^{-1}$). We discuss possible origins in Section

Discussion. In contrast, the Trivial sample does not show any clear linear one-dimensional contribution, confirming the absence of edge transport in the gap (Fig.4a and 4d). We however note the scaling analysis can hardly be performed for negative energies. Indeed, c_q varies abruptly, and errors and variations in the determination of C_g are amplified in this regime especially for Trivial as the QW is strongly depleted in the gap.

After identifying the presence of a one-dimensional quantum capacitance c_q^{1D} near the gap of the QW from the length dependence of C_q, we now turn to the study of the full high-frequency spectrum of the complex admittance $Y(\omega)$. As the characteristic RC timescales of the one- and two-dimensional components differ, we show below that we can distinguish their respective signatures in this high-frequency regime. Indeed, near the gap of topological samples, the microwave spectrums exhibit striking two-mode dynamical transport which strongly departs from that of a single distributed RC line.

High frequency regime

Using a VNA and standard de-embedding techniques (see Methods), we have measured the complex admittance $Y(\omega)$ of the capacitors up to frequencies largely exceeding the charge relaxation frequency $1/2\pi RC$ of the device, typically $1\,\text{GHz}$ for $L = 10\,\mu\text{m}$. In this high-frequency regime, propagation effects cannot be neglected, and the capacitors host evanescent waves[20,23,33], driven by the resistance of the HgTe film. Assuming translation invariance along the transverse axis, the admittance of the capacitor reads (see SI):

$$Y(\omega) = \frac{1}{1/R_c + \frac{ik}{R}\tanh(ik)} \qquad (2)$$

where R_c describes the lumped contact resistance, while the tanh term describes the evanescent waves in the capacitor (with $k = \sqrt{iRC_t\omega}$).

The fits obtained with this simple model yields an excellent agreement in a a wide range of energies corresponding mostly to the valence and conduction band as illustrated in Fig.5a and 5b. The low frequency part (Fig.5a) in particular validates the expansion used in the low-frequency regime. The high frequency regime confirms the evanescent regime, and yields the value of the HgTe sheet resistance R and of the contact resistance R_c. R_c is found to be relatively independent of V_g in the validity range of the model, with $R_c = 0.3 - 4\,\text{k}\Omega$ depending on sample, slightly higher for non-inverted than for topological samples. However, in Topological A and B, we observe strong discrepancies arising near the gap between this simple one-carrier model and the data as illustrated in Fig.5c and 5d. In particular, the admittance Y exhibits two successive low-frequency regimes (DC-0.2 GHz and 0.2-0.8 GHz). We attribute these features to the presence of two independent types of charge carriers, namely the bulk (2D) and edge (1D carries), in
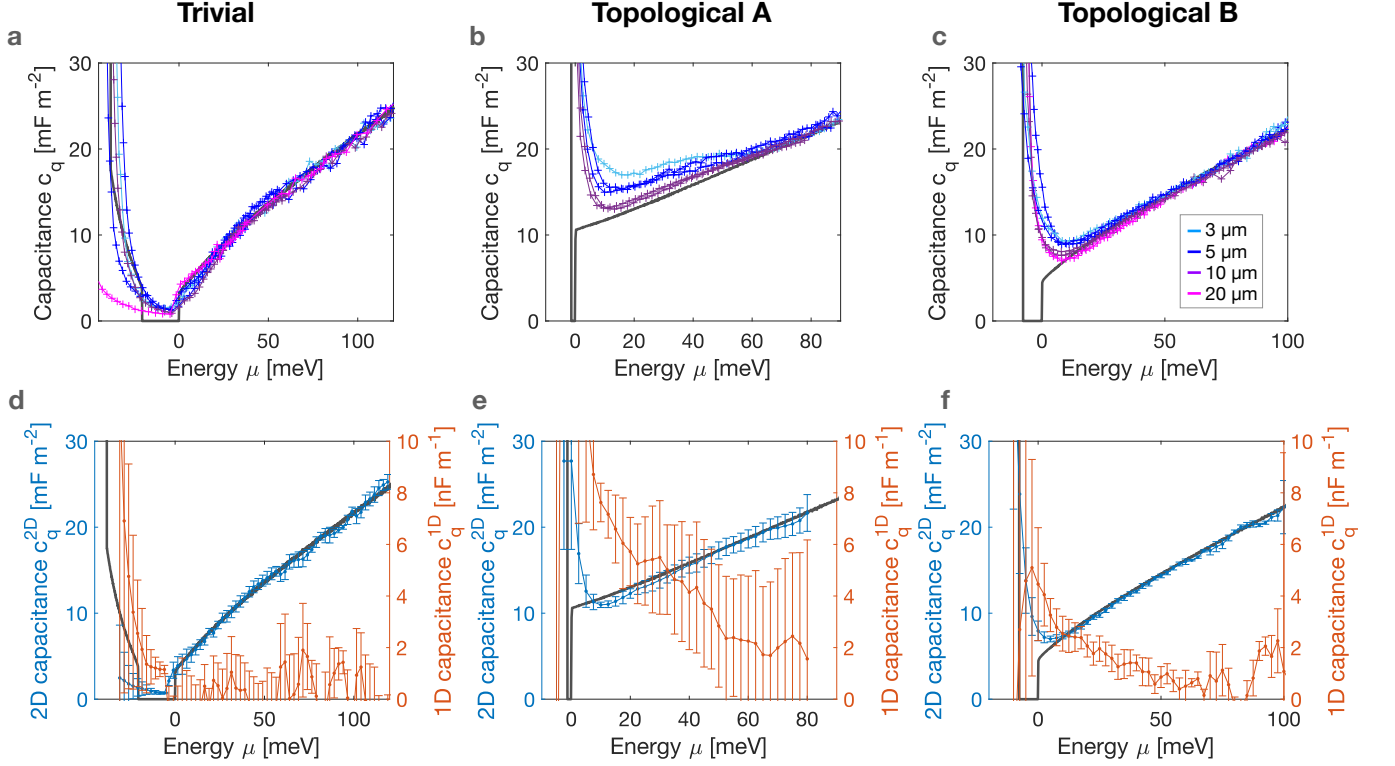
FIG. 4. **Length dependence of the quantum capacitance:** a, b, c) Quantum capacitance c_q (per unit area) as function of energy μ measured for different lengths $L = 3, 5, 10, 20\,\mu\text{m}$. The grey line corresponds to the computed value of c_q given the $\mathbf{k} \cdot \mathbf{p}$ band structure, the colored lines correspond to experimental data for a size L indicated by the caption d, e, f) On the left axis, two-dimensional component c_q^{2D} (per unit area) as a blue line, the grey line corresponds to c_q computed from the $\mathbf{k} \cdot \mathbf{p}$ band structure. On the right axis, one-dimensional component c_q^{1D} (per unit length) as a red line.

accordance with the results of the low-frequency analysis, with different charge relaxation times. Consequently, we model the system using two parallel distinct distributed RC circuits, each with a contact resistance:

$$Y(\omega) = Y^{1D}(\omega) + Y^{2D}(\omega) \qquad (3)$$

where $Y^{1D/2D}$ are both given by Eq.(2). We obtain an excellent agreement between model and data over the full frequency range (Fig.5c and 5d) and the two low-frequency regimes are fully captured. However the fits can efficiently be performed only in a small region of energies, for which the two circuits are sufficiently distinguishable. The results are shown in Fig.6a. The largest contribution c_q^{2D} is attributed to the two-dimensional bulk states and is observed to follow the $\mathbf{k} \cdot \mathbf{p}$ predictions. Additionally the small contribution of the second carrier is observed to grow close to the gap is consequently attributed to c_q^{1D}. Its order of magnitude in the gap $c_q^{1D} \simeq 10\,\text{nF}\,\text{m}^{-1}$ is compatible with the results obtained from the low-frequency length dependence, thus validating our analysis. Our measurement technique is primarily sensitive to capacitances. Consequently, though the contact and sheet resistances can easily be separated in the single-carrier model, they can only be determined with an accuracy of typically 50% in the two-carrier model.

We observe nonetheless that, near the gap, the total 2D resistance $R_t^{2D} \simeq 40\,\text{k}\Omega$ is much larger than the total 1D resistance $R_t^{1D} \simeq 10 - 15\,\text{k}\Omega$. Moreover, the analysis gives access to the charge relaxation times and frequencies (given respectively by $\tau_{1D/2D} = R_t^{1D/2D}C_t^{1D/2D}$ and $f_{1D/2D} = 1/2\pi\tau_{1D/2D}$), as plotted in Fig.6b. In the conduction band, where the single-mode picture holds, we observe that the (bulk) electrons have a short charge relaxation time ($\tau_{2D} \simeq 0.23\,\text{ns}$) or equivalently a high response frequency ($f_{2D} \simeq 0.7\,\text{GHz}$). However, this charge relaxation time increases drastically when the Fermi level approaches the gap and reaches $\tau_{2D} \simeq 1.5\,\text{ns}$ ($f_{2D} \simeq 0.1\,\text{GHz}$). In the same energy range, the second contribution, attributed to the edge electrons, yields a short response time $\tau_{1D} \simeq 0.17\,\text{ns}$ ($f_{1D} \simeq 0.9\,\text{GHz}$).

Together, the analysis of the capacitances and charge relaxation times substantiates and sharpens the picture obtained in the low-frequency regime near the gap, with a small edge DOS with 'fast' electrons and rather high conductance, atop a very dense but resistive and 'slow' bulk background. In the last section, we summarize the results obtained from both the low- and high-frequency methods and discuss their outreach in the perspective of improving the transport quality of topological edge states.
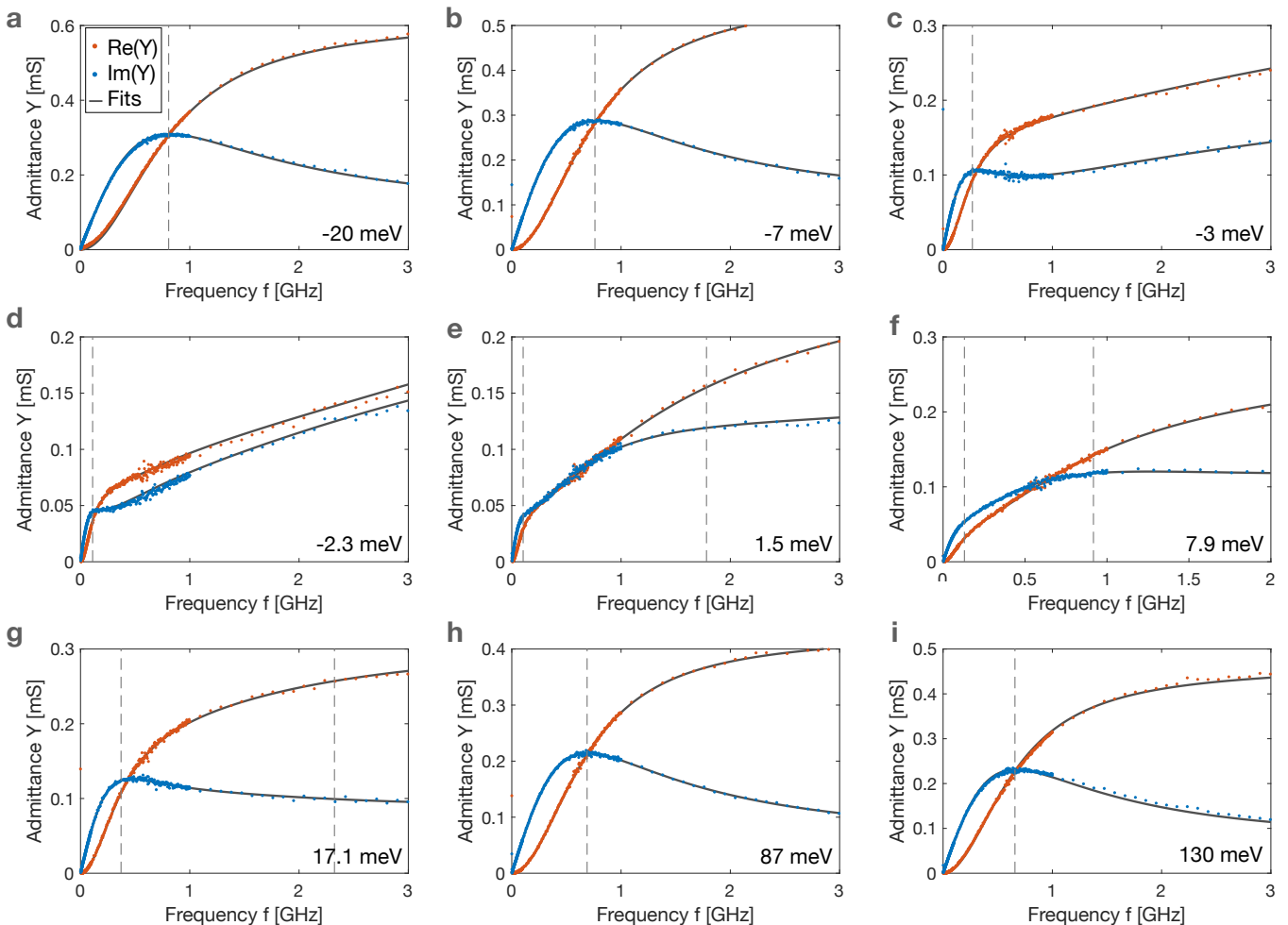
FIG. 5. **High-frequency admittance:** Admittance Y as function of frequency f in the $\mathrm{DC} - 3\,\mathrm{GHz}$ for different energies μ, obtained on sample Topological B for $L = 5\,\mu\mathrm{m}$. The value of μ is indicated in each panel. Panels a,b correspond to the conduction band, h and i to the valence band, and show a good agreement with a single-mode model. The other panels (c, d, e, f, g) correspond to the transition from valence to conduction bands, according to the band structure in Fig.6. They exhibit a different spectrum, with two low-frequency regimes, and are only well fitted by the two-mode model. The best fits (either single- or two-mode) are shown as a grey line in all panels. The vertical dashed lines indicate the values of the charge relaxation frequencies f_{2D}, and f_{1D} (when in the frequency range, panels e, f, g).

DISCUSSION

The study of capacitors unveils a precise and surprising description of the density of states in the two-dimensional topological insulator HgTe. A one-dimensional component can be detected near the gap of the QW only in inverted (topological) heterostructures, so that it is thus likely to originate from the topological edge states. This one-dimensional DOS coexists with the conduction band over a large range of energies (roughly $50\,\mathrm{meV}$), in line with theoretical predictions[34] and observations[6,35]. However it is partially obscured by the very large DOS of the two-dimensional bulk when approaching the gap. In fact, in topological samples (such as Topological A and B), the gap is clearly indicated by a maximum in resistance R_t, but corresponds to a large DOS, whereas the minimum in the DOS is often located above the gap ($\mu \simeq 5 - 10\,\mu\mathrm{eV}$). This configuration is likely to be the result of disorder or inhomogeneous electrostatics in the samples, yielding charge puddles which pin the Fermi energy in the valence bands, and smear out the very heavy valence band over an energy scale of 10 to $30\,\mathrm{meV}$. The bulk is, as expected, found to be rather resistive in the gap. It may still however influence the conductance, for example in Josephson junctions for which the aspect ratio favors it. Hence, our observations explain a posteriori why the fractional Josephson effect in HgTe has been observed to be stronger in the conduction band than in the gap[6,7]. As this very large two-dimensional DOS near the gap directly results from the very heavy valence band, band structure engineering as tested on HgTe[36] may help reducing the amount of states in the bulk.
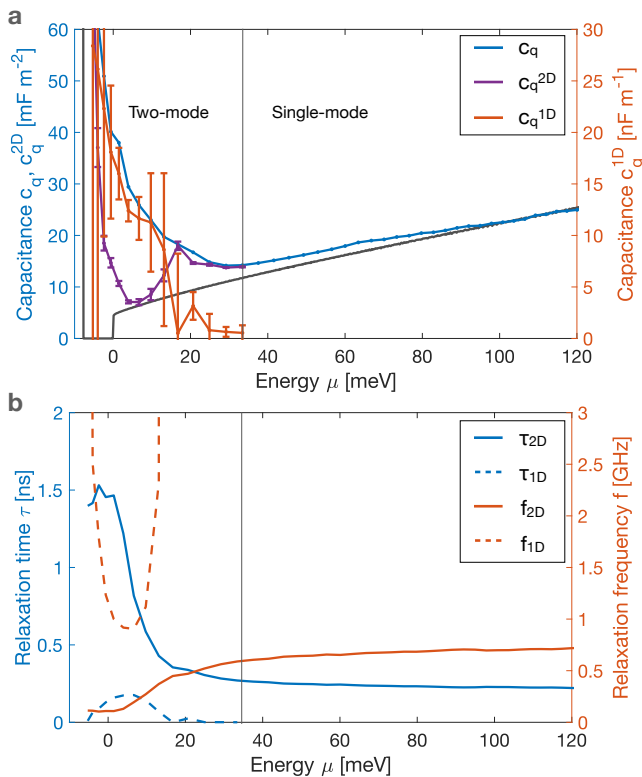
FIG. 6. **Quantum capacitances and charge relaxation times/frequencies:** On the left axis, the total quantum capacitance c_q is plotted in blue. The capacitance of the largest electron system c_q^{2D} attributed to the 2D bulk carriers, is shown alongside in purple. The prediction of the $\mathbf{k} \cdot \mathbf{p}$ calculations are shown as a solid grey line. The small contribution attributed to the 1D electron system c_q^{1D} is plotted on the right axis.

Our observations also directly points to very dense edge states, with a quantum capacitance c_q^{1D} about 25-50 times larger than the naive theoretical value. Though we can not at this stage clearly establish the most relevant mechanism, several scenarios can be proposed. First, we note that high quantum capacitances have also been measured for quantum Hall edge states[37,38], and have been attributed to edge reconstruction under the action of electrostatics and electron-electron interactions[39,40]. Such mechanisms lead to the formation of so-called compressible and incompressible stripes and could similarly play a role and even be responsible for backscattering in the edge states[41] but remain however rather unlikely as the observed capacitances[38] were inferior to $1\,\mathrm{nF\,m^{-1}}$. The resistance of the edge states seems slightly larger than predicted and suggests the scenario of helical edge states coupled to scattering centers rather than the presence of additional conduction channels[42]. The observed situation may originate in the presence of residual charge puddles in the bulk, to which the edge states could couple, thus introducing some scattering and drastically increasing the capacitance of the edges. These puddles can

be the result of disorder, especially when the gap of the QW is small. The puddles have been suggested as a potential source of scattering[14] and could be identified via specific signatures in the noise[43]. However, Eq.(1) assumes a uniform puddle density c_q^{2D}, and thus strongly suggests that the charge density is larger close to the edges of the sample. Gate electrostatics could play an important role and enhance the creation of electron pockets confined near the edges as the topological edge states themselves may screen the action of the gate. Regardless of the microscopic details, one can estimate that a (spin-degenerate) bulk sub-band, could contribute up to $5\,\mathrm{nF\,m^{-1}}$, so that typically 1 to 2 states would reside in the vicinity of the topological edge states.

Finally, we point out that very dissimilar time-scales rule the electronic transport of the one- and two-dimensional states near the gap regions, with charge relaxation times such that $\tau_{2D} \simeq 9\,\tau_{1D}$. This suggests that a careful choice of the drive frequency would allow for addressing dynamically the edge states on time-scales over which the bulk states are frozen. Our results confirms the interest of microwaves for investigating the physics of topological edge states, and in particular the peculiar Luttinger liquid behavior[32,45–47] which is more naturally unveiled at finite frequencies[48,49].

In a nutshell, our measurements bring up new information on the microscopic details of topological edge states. While the bulk is mostly insulating in the gap, its DOS is very large and may obscure that of the edges. Most strikingly, the edge states are found to be rather dense which suggests that they consist of topological edge states dressed by other states, which contribute to the large DOS and to scattering, but not in a significant manner to transport. This scenario highlights the interplay of charge disorder and gate electrostatics with the physics of edge states, and is inherent to the physics of QSH edge states. Thus, this work opens new directions in the search for robust topological systems, for example the development of lateral gates to control the electrostatic potential near the edges, or the dynamical addressing of the edge states. We also believe that our observations call for in-depth theoretical modeling of QSH edges. The idealized homogeneous insulating bulk is hardly achieved in practice in a topological insulator, which calls for an electrostatic model of the bulk and edge states as a prerequisite robust topological edges states suitable for topological quantum computation or spinorbitronics.

METHODS

Experimental techniques

The measurements have been performed in a microwave cryogenic probe station Janis ST-500 equipped with Picoprobe GSG-100 microwave probes. The low-frequency measurements rely on a lock-in detector (Zurich Instruments HF2LI) combined with a low-noise

pre-amplifier. For high-frequency phase-referenced measurements, we use a Vector Network Analyzer (VNA) Anritsu MS4640. The VNA is first calibrated in the desired frequency range using the SOLT (short-open-load-thru) method on a calibration substrate Picoprobe CS5, thus moving the reference planes to the microwave probe ends. The propagation in the contacts is further corrected by measuring the response of a thru-line. Finally, stray capacitances are subtracted by measuring a dummy device with identical geometry but without the conductive HgTe mesa structure.

Length dependence

When in the gap, the quantum capacitance c_q exhibits a length dependence, suggesting that the surface (total surface $S_t = L^2$) is split in two parts :

- the edges, surface $S_1 = 3WL - 2W^2 \simeq 3WL$

- the bulk, surface $S_2 = (L-W)(L-2W) = S_t - S_1$

where W is the width of the edge states. The edge states are assumed to run on three sides only of the gated surface L^2, but not on the side nearby the contact. We assume a geometric capacitance $C_g = c_g L^2$, in series with the two quantum capacitances $c_{q1}S_1$ and $c_{q2}S_2$ in parallel:

$$C_q = c_{q1}S_1 + c_{q2}S_2 \qquad (4)$$
$$= c_q^{2D}L^2 + 3c_q^{1D}L \qquad (5)$$

with $c_q^{2D} = c_{q1}$ and $c_q^{1D} = W(c_{q2} - c_{q1})$.

The total capacitance is then given by, using the assumption $\frac{3Lc_q^{1D}}{c_q^{2D}L^2} \ll 1$,

$$C_t = \frac{C_q C_g}{C_g + C_q} \qquad (6)$$
$$= c_t^{2D}L^2 + 3c_t^{1D}L \qquad (7)$$

with $c_t^{2D} = \frac{c_q^{2D}c_g}{c_g + c_q^{2D}}$ and $c_t^{1D} = c_q^{1D}\left(\frac{c_t^{2D}}{c_q^{2D}}\right)^2$. These expressions can be used to compute c_q^{2D} and c_q^{1D} in the two-carrier model.

DATA AVAILABILITY

The data sets generated and/or analyzed during the current study are available from the corresponding author on reasonable request.

ACKNOWLEDGMENTS

AUTHOR CONTRIBUTIONS

M.C.D., S.H., A.G. and H.Ba. performed the measurements. S.H. and K.B. fabricated the samples, based on MBE layers grown by R.S. and L.L. E.B. supervised the project. All authors participated to the analysis of the results and to the writing of the manuscript.

[1] M. Konig, S. Wiedmann, C. Brune, A. Roth, H. Buhmann, L. W. Molenkamp, X.-L. Qi, and S.-C. Zhang, Science **318**, 766 (2007).

[2] A. Roth, C. Brune, H. Buhmann, L. W. Molenkamp, J. Maciejko, X.-L. Qi, and S.-C. Zhang, Science **325**, 294 (2009).

[3] C. Brüne, A. Roth, H. Buhmann, E. M. Hankiewicz, L. W. Molenkamp, J. Maciejko, X.-L. Qi, and S.-C. Zhang, Nature Physics **8**, 485 (2012).

[4] G. M. Gusev, A. D. Levin, Z. D. Kvon, N. N. Mikhailov, and S. A. Dvoretsky, Physical Review Letters **110** (2013), 10.1103/PhysRevLett.110.076805.

[5] M. R. Calvo, F. de Juan, R. Ilan, E. J. Fox, A. J. Bestwick, M. Mühlbauer, J. Wang, C. Ames, P. Leubner, C. Brüne, S. C. Zhang, H. Buhmann, L. W. Molenkamp, and D. Goldhaber-Gordon, Physical Review Letters **119** (2017), 10.1103/PhysRevLett.119.226401.

[6] E. Bocquillon, R. S. Deacon, J. Wiedenmann, P. Leubner, T. M. Klapwijk, C. Brüne, K. Ishibashi, H. Buhmann, and L. W. Molenkamp, Nature Nanotechnology **12**, 137 (2016).

[7] R. S. Deacon, J. Wiedenmann, E. Bocquillon, F. Domínguez, T. M. Klapwijk, P. Leubner, C. Brüne, E. M. Hankiewicz, S. Tarucha, K. Ishibashi, H. Buhmann, and L. W. Molenkamp, Physical Review X **7** (2017), 10.1103/PhysRevX.7.021011.

[8] I. Knez, R.-R. Du, and G. Sullivan, Physical Review Letters **107** (2011), 10.1103/PhysRevLett.107.136603.

[9] L. Du, I. Knez, G. Sullivan, and R.-R. Du, Physical Review Letters **114** (2015), 10.1103/PhysRevLett.114.096802.

[10] F. Reis, G. Li, L. Dudy, M. Bauernfeind, S. Glass, W. Hanke, R. Thomale, J. Schäfer, and R. Claessen, Science **357**, 287 (2017).

[11] S. Wu, V. Fatemi, Q. D. Gibson, K. Watanabe, T. Taniguchi, R. J. Cava, and P. Jarillo-Herrero, Science **359**, 76 (2018).

[12] K. Bendias, S. Shamim, O. Herrmann, A. Budewitz, P. Shekhar, P. Leubner, J. Kleinlein, E. Bocquillon, H. Buhmann, and L. W. Molenkamp, Nano Letters (2018), 10.1021/acs.nanolett.8b01405.

[13] F. Crépin, J. C. Budich, F. Dolcini, P. Recher, and B. Trauzettel, Physical Review B **86** (2012), 10.1103/PhysRevB.86.121106.

[14] J. I. Väyrynen, M. Goldstein, Y. Gefen, and L. I. Glazman, Physical Review B **90** (2014), 10.1103/PhysRevB.90.115309, arXiv:1406.6052.

[15] S. Essert, V. Krueckl, and K. Richter, Physical Review B **92** (2015), 10.1103/PhysRevB.92.205306, arXiv:1507.00928.

[16] A. Mani and C. Benjamin, Physical Review Applied **6** (2016), 10.1103/PhysRevApplied.6.014003.

[17] C.-H. Hsu, P. Stano, J. Klinovaja, and D. Loss, Physical Review B **96** (2017), 10.1103/PhysRevB.96.081405.

[18] S. Xu, Y. Han, X. Chen, Z. Wu, L. Wang, T. Han, W. Ye, H. Lu, G. Long, Y. Wu, J. Lin, Y. Cai, K. M. Ho, Y. He, and N. Wang, Nano Letters **15**, 2645 (2015).

[19] D. A. Kozlov, D. Bauer, J. Ziegler, R. Fischer, M. L. Savchenko, Z. D. Kvon, N. N. Mikhailov, S. A. Dvoretsky, and D. Weiss, Physical Review Letters **116** (2016), 10.1103/PhysRevLett.116.166802.

[20] A. Inhofer, S. Tchoumakov, B. A. Assaf, G. Fève, J. M. Berroir, V. Jouffrey, D. Carpentier, M. O. Goerbig, B. Plaçais, K. Bendias, D. M. Mahler, E. Bocquillon, R. Schlereth, C. Brüne, H. Buhmann, and L. W. Molenkamp, Physical Review B **96** (2017), 10.1103/PhysRevB.96.195104.

[21] A. Inhofer, J. Duffy, M. Boukhicha, E. Bocquillon, J. Palomo, K. Watanabe, T. Taniguchi, I. Estève, J. M. Berroir, G. Fève, B. Plaçais, and B. A. Assaf, Physical Review Applied **9** (2018), 10.1103/PhysRevApplied.9.024022.

[22] B. A. Bernevig, T. L. Hughes, and S.-C. Zhang, Science **314**, 1757 (2006).

[23] E. Pallecchi, A. C. Betz, J. Chaste, G. Fève, B. Huard, T. Kontos, J.-M. Berroir, and B. Plaçais, Physical Review B **83** (2011), 10.1103/PhysRevB.83.125408.

[24] C. N. Berglund, IEEE Transactions on Electron Devices **ED-13**, 701 (1966).

[25] E. G. Novik, A. Pfeuffer-Jeschke, T. Jungwirth, V. Latussek, C. R. Becker, G. Landwehr, H. Buhmann, and L. W. Molenkamp, Physical Review B **72** (2005), 10.1103/PhysRevB.72.035321, arXiv:cond-mat/0409392.

[26] J. Chaste, L. Lechner, P. Morfin, G. Fève, T. Kontos, J.-M. Berroir, D. C. Glattli, H. Happy, P. Hakonen, and B. Plaçais, Nano Letters **8**, 525 (2008).

[27] G. Tkachov, C. Thienel, V. Pinneker, B. Buettner, C. Bruene, H. Buhmann, L. W. Molenkamp, and E. M. Hankiewicz, Physical Review Letters **106** (2011), 10.1103/PhysRevLett.106.076802, arXiv:1101.5692.

[28] M. Büttiker, H. Thomas, and A. Prêtre, Physics Letters A **180**, 364 (1993), buttiker1993.

[29] J. Gabelli, G. Fève, J.-M. Berroir, B. Plaçais, A. Cavanna, B. Etienne, Y. Jin, and C. Glattli, Science **313**, 499 (2006), arXiv:cond-mat/0610572.

[30] J. Gabelli, G. Fève, J.-M. Berroir, and B. Plaçais, Reports on Progress in Physics **75**, 126504 (2012).

[31] S. E. Nigg and M. Buttiker, Physical Review B **77** (2008), 10.1103/PhysRevB.77.085312, arXiv:0709.3956.

[32] T. Müller, R. Thomale, B. Trauzettel, E. Bocquillon, and O. Kashuba, Physical Review B **95** (2017), 10.1103/PhysRevB.95.245114, arXiv:1701.03050.

[33] H. Graef, D. Mele, M. Rosticher, L. Banszerus, C. Stampfer, T. Taniguchi, K. Watanabe, E. Bocquillon, G. Fève, J.-M. Berroir, E. H. T. Teo, and B. Plaçais, Journal of Physics: Materials **1**, 01LT02 (2018).

[34] X. Dai, T. L. Hughes, X.-L. Qi, Z. Fang, and S.-C. Zhang, Physical Review B **77** (2008), 10.1103/PhysRevB.77.125319.

[35] K. C. Nowack, E. M. Spanton, M. Baenninger, M. König, J. R. Kirtley, B. Kalisky, C. Ames, P. Leubner, C. Brüne, H. Buhmann, L. W. Molenkamp, D. Goldhaber-Gordon, and K. A. Moler, Nature Materials **12**, 787 (2013).

[36] P. Leubner, L. Lunczer, C. Brüne, H. Buhmann, and L. W. Molenkamp, Physical Review Letters **117** (2016), 10.1103/PhysRevLett.117.086403, arXiv:1608.01581.

[37] S. Takaoka, K. Oto, H. Kurimoto, K. Murase, K. Gamo, and S. Nishi, Physical Review Letters **72**, 3080 (1994).

[38] S. Takaoka, K. Oto, S. Uno, K. Murase, F. Nihey, and K. Nakamura, Physical Review Letters **81**, 4700 (1998).

[39] D. B. Chklovskii, B. I. Shklovskii, and L. I. Glazman, Physical Review B **46**, 4026 (1992).

[40] C. d. C. Chamon and X. G. Wen, Physical Review B **49**, 8227 (1994).

[41] J. Wang, Y. Meir, and Y. Gefen, Physical Review Letters **118** (2017), 10.1103/PhysRevLett.118.046801, arXiv:1609.07700.

[42] N. Kumada, P. Roulleau, B. Roche, M. Hashisaka, H. Hibino, I. Petković, and D. C. Glattli, Physical Review Letters **113** (2014), 10.1103/PhysRevLett.113.266601.

[43] J. I. Väyrynen, D. I. Pikulin, and J. Alicea, Physical Review Letters **121** (2018), 10.1103/PhysRevLett.121.106601.

[44] S. Tchoumakov, V. Jouffrey, A. Inhofer, E. Bocquillon, B. Plaçais, D. Carpentier, and M. O. Goerbig, Physical Review B **96** (2017), 10.1103/PhysRevB.96.201302, arXiv:1704.08954.

[45] C. Wu, B. A. Bernevig, and S.-C. Zhang, Physical Review Letters **96** (2006), 10.1103/PhysRevLett.96.106401.

[46] A. Calzona, M. Carrega, G. Dolcetto, and M. Sassetti, Physical Review B **92** (2015), 10.1103/PhysRevB.92.195414.

[47] G. Dolcetto, M. Sassetti, and T. L. Schmidt, arXiv:1511.06141 [cond-mat] (2015), 10.1393/ncr/i2016-10121-7, arXiv:1511.06141 [cond-mat].

[48] E. Bocquillon, V. Freulon, J.-M. Berroir, P. Degiovanni, B. Plaçais, A. Cavanna, Y. Jin, and G. Fève, Nature Communications **4** (2013), 10.1038/ncomms2788, arXiv:1309.5610.

[49] H. Kamata, N. Kumada, M. Hashisaka, K. Muraki, and T. Fujisawa, Nature Nanotechnology **9**, 177 (2014).

Dressed topological edge states in HgTe-based 2D topological insulators
–
Supplementary Online Material

I.   FROM C_t TO c_q

The measurements with a lock-in amplifier or a VNA directly yields the total capacitance C_t of the sample. An example measurement of C_t as function of V_g is shown in Fig.7a. The gap feature is immediately visible around $V_g \simeq 0.1\,\mathrm{V}$ as a dip in C_t. The contrast is very good (typically 25 % modulation of C_t) thanks to the very thin insulator layer that maximizes the value of C_t. A clear saturation is observed for $V_g < -0.2\,\mathrm{V}$ that signals the very heavy valence band, for which $C_t \simeq C_g$. From the saturation value, we obtain C_g with an estimated error $< 2\%$. Knowing C_g, we compute C_q and $c_q = \frac{C_q}{S}$, where S is the area of the sample. To avoid any systematic error in c_q, we measure S with microscope pictures. In the length dependence (see Main article), we use $\sqrt{S}$ rather than the nominal value L. Despite the accuracy of less than 2% on C_g, the agreement with $\mathbf{k} \cdot \mathbf{p}$ prediction can sometimes be mediocre. For simplicity, we take these theoretical predictions as a reference and thus fine tune the value of C_g (within 2%) to obtain the best agreement, and finally obtain the plot of c_q as function of μ as presented in Fig.7

II.   HIGH FREQUENCY ADMITTANCE

Following earlier works[20,23], we model the capacitor as a distributed RC line (of length L along the x axis, see Main text). On the source side, an oscillating voltage $V_{ac}(t)$ is applied, while a dc gate voltage is set to the other end of the line. Solving the Kirchhoff equations, one can easily show that the local voltage $V(x)$ and current $I(x)$ read :

$$V(x) = V_+ e^{i\gamma x} + V_- e^{-i\gamma x} \tag{8}$$

$$I(x) = \frac{i\gamma}{r}\left(V_+ e^{i\gamma x} + V_- e^{-i\gamma x}\right) \tag{9}$$

with $\gamma = \sqrt{i\omega \mathcal{R} \mathcal{C}_t}$. Solving for the above mentioned boundary conditions, this immediately yields the admittance $Y_0(\omega)$ of the line:

$$Y_0(\omega) = \frac{I(0)}{V(0)} = \frac{i\gamma}{r}\tanh(i\gamma L) = \frac{ik}{R}\tanh(ik) \tag{10}$$

with $k = \sqrt{i\omega RC_t}$, $R = \mathcal{R}L, C_t = \mathcal{C}_t L$. Taking into account the contact resistance between the QW and the gold lead of the source, a discrete resistance R_c is further attached to one end and the admittance Y is finally given by:

$$Y(\omega) = \frac{1}{1/R_c + Y_0(\omega)} = \frac{1}{1/R_c + \frac{ik}{R}\tanh(ik)} \tag{11}$$

The low frequency expansion of $Y(\omega)$ can then be calculated, and gives:

$$Y(\omega) = i\omega C + \omega^2 R_t C^2 + o(\omega^2) \tag{12}$$

with $R_t = R_c + \frac{R}{3}$.

III.   EXAMPLE RF SPECTRUM

In this section, we show how the single-mode model fails to describe the spectra measured near the gap. In Fig.8, we first present data taken in the conduction band (Fig.8a and 8b), showing perfect agreement with the single-mode fit. In Fig.8c and 8d, the single-mode fit fails to describe data taken near the gap (dashed line) while a two-mode fit accounts for the observation of two distinct charge relaxation times.
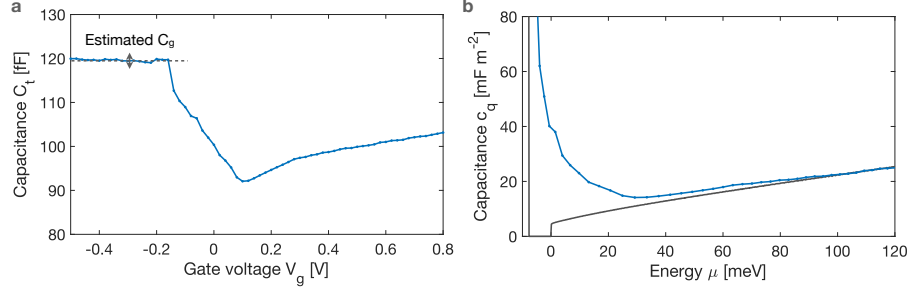
FIG. 7. **Quantum capacitances of the two electron systems:** On the left axis, the total quantum capacitance c_q is plotted in blue. The capacitance of the largest electron system c_q^{2D} attributed to the 2D bulk carriers, is shown alongside in purple. The prediction of the $\mathbf{k} \cdot \mathbf{p}$ calculations are shown as a solid grey line.
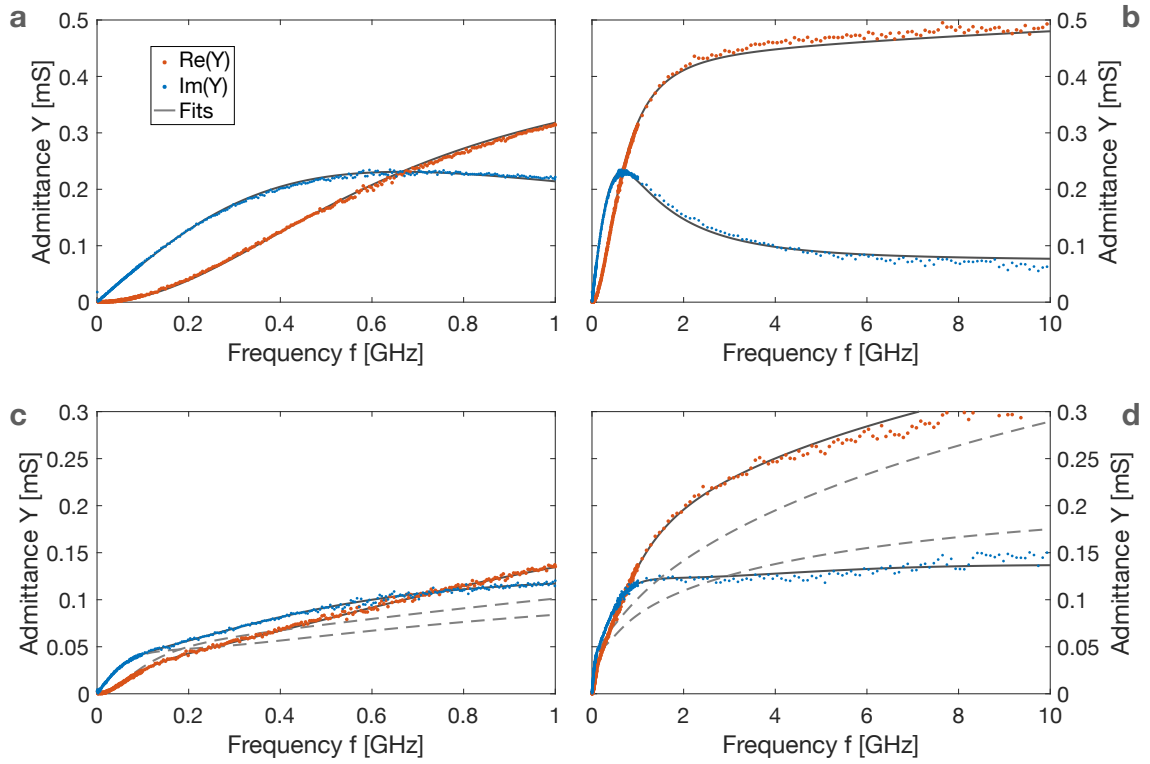

FIG. 8. **Microwave admittance:** a,b) Microwave admittance Y as function of frequency f measured in the conduction band shown as blue and red dots, showing a very good agreement with the single-mode model (shown as a dark grey line) c,d) Microwave admittance Y as function of frequency f measured near the gap. It shows a very good agreement with the two-mode model (shown as a dark grey line), while the single-mode model fails to reproduce the observed behaviors (dashed lines).